Journal of Solid State Chemistry 183 (2010) 2127–2132

Contents lists available at ScienceDirect

Journal of Solid State Chemistry

journal homepage: www.elsevier.com/locate/jssc

Quantitative determination of site occupancy of multi-rare-earth elements doped into Ca_2SnO_4 phosphor by electron channeling microanalysis

Y. Fujimichi [a], S. Muto [a,*], K. Tatsumi [a], T. Kawano [b], H. Yamane [b]

[a] Graduate School of Engineering, Nagoya University, Nagoya 464-8603, Japan
[b] Institute of Multidisciplinary Research for Advanced Materials, Tohoku University, Sendai 980-8577, Japan

ARTICLE INFO

Article history:
Received 18 May 2010
Received in revised form
13 July 2010
Accepted 16 July 2010
Available online 4 August 2010

Keywords:
Rare-earth dopant
Transmission electron microscopy
Energy-dispersive X-ray analysis
Electron energy-loss spectroscopy
Electron channeling

ABSTRACT

X-ray fluorescence analysis based on electron channeling effects in transmission electron microscopy (TEM) was performed on Ca_2SnO_4 phosphor materials doped with Eu^{3+}/Y^{3+} at various concentrations, which showed red photoluminescence associated with the $^5D_0$–$^7F_2$ electric dipole transition of Eu^{3+} ions. The method provided direct information on which host element site dopant elements occupy, the results of which were compared with those of X-ray diffraction (XRD)–Rietveld analysis. The obtained results indicated that while it is not favorable for a part of Eu^{3+} to occupy the smaller Sn^{4+} site, this is still energetically better than creating Ca vacancies or any other of the possible charge balance mechanisms. The local lattice distortions associated with dopant impurities with different ionic radii were also examined by TEM–electron energy-loss spectroscopy (TEM–EELS). The change in PL intensity as a function of dopant concentration is discussed based on the experimental results, although the general concept of concentration quenching applies.

1. Introduction

Various types of oxide ceramic phosphors have been synthesized by doping rare-earth activators into phosphor host materials [1]. To obtain efficient luminescence from the synthesized phosphors, it is important to control the type and amount of atomic site that dopant rare-earth elements occupy. It is also crucial to ensure that dopant impurities substitute for the host atom at the correct site as designed or to quantitatively measure the fraction of dopants that occupy crystallographic atomic sites. Diffraction techniques (X-ray and neutron diffraction analyses) with Rietveld analysis have been generally applied for these purposes, although they do not always work well when the scattering powers of the host elements and impurities are not markedly different from each other or when structural information available for fitting constraints is not sufficient to reduce the degree of freedom for good convergence.

Chen et al. [2] and Yang et al. [3] reported that Eu^{3+}-doped Ca_2SnO_4 exhibits strong photoluminescence (PL) derived from the $^5D_0$–$^7F_2$ electric dipole transition of Eu^{3+} ions. They regarded Eu^{3+} as being doped only at the Ca site of Ca_2SnO_4, where in both cases Ca vacancies were proposed to maintain charge balance. When just considering ionic radii it is logical to assume that the Eu^{3+} (whose ionic radii are 1.01 and 0.95 Å when 7- and 6-coordinated with oxygen [4]) all goes onto the Ca^{2+} sites (1.06 Å [4]) since Eu^{3+} is much closer in size to Ca^{2+} than to Sn^{4+} (0.69 Å [4]). Chen et al. presented the solution limit of Eu (x) at $x=0.07$ for $(Ca_{1-x}Eu_x)_2SnO_4$ (but it may be better to denote as $(Ca_{1-1.5x}Eu_x)_2SnO_4$, taking Ca vacancies into account) by X-ray powder diffraction, the chemical formula of which takes the charge balance into account instead of considering the possibility that some Sn^{4+} could be reduced to Sn^{2+}. After these studies, however, solid state reaction synthesis and Rietveld analysis of powder X-ray diffraction (XRD) pattern by Yamane et al. revealed that Eu^{3+} equally occupies both the Ca^{2+} and Sn^{4+} sites [5]. The solid solution range of $Ca_{2-x}Eu_{2x}Sn_{1-x}O_4$ was shown to be $0<x\leq 0.3$. PL intensity decreased with Eu concentration when the Eu concentration x exceeds 0.1 [5], which has generally been explained by the concept of concentration quenching. The same authors' group also prepared a Eu and Y co-doped sample $Ca_{1.8}Y_{0.2}Eu_{0.2}Sn_{0.8}O_4$, based on the idea that Y^{3+} ions with a smaller ionic radius preferentially occupy smaller cation (Sn^{4+}) sites, driving larger Eu^{3+} ions out of the Sn^{4+} site into the larger Ca^{2+} site [5]. $Ca_{1.8}Y_{0.2}Eu_{0.2}Sn_{0.8}O_4$ exhibited a stronger PL intensity than the Eu-doped sample $Ca_{1.9}Eu_{0.2}Sn_{0.9}O_4$, both of which had the same Eu content in the formulae. The stronger PL in the codoped sample is explained by the increased fraction of Eu^{3+} ions occupying the Ca site, because the Ca site is coordinated by seven oxygen atoms, the asymmetric configuration of which enhances the electric dipole moment, compared with the symmetric six-coordinated Sn site. XRD–Rietveld analysis confirmed that preferential Ca^{2+} site occupation by Eu^{3+} and Sn^{4+} site occupation by Y^{3+} provide a small goodness-of-fit indicator of the Rietveld fit in the codoped samples [6], although it is not

* Corresponding author. Fax: +81 52 789 4684.
E-mail address: s-mutoh@nucl.nagoya-u.ac.jp (S. Muto).

0022-4596/$ - see front matter © 2010 Elsevier Inc. All rights reserved.
doi:10.1016/j.jssc.2010.07.026

possible to determine the fraction of Eu(Y) that actually occupies the $Ca^{2+}(Sn^{4+})$ site. In this respect, it is important to quantitatively determine the site occupancies of this series of materials.

In this study, a series of Eu and Y codoped samples with various dopant concentrations were synthesized and the site occupancies of rare-earth dopants were directly determined by X-ray fluorescence spectroscopy (energy-dispersive X-ray analysis (EDXA)) combined with transmission electron microscopy (TEM), and the local spatial and electronic structure changes were also examined by electron energy loss spectroscopy (EELS).

2. Material and methods

2.1. Sample synthesis and X-ray characterization

Starting powders of $CaCO_3$ (99.99%, Rare metallic), SnO_2 (99.9%, Sigma–Aldrich), Eu_2O_3 (99.99%, Shin-Etsu Chem.) and Y_2O_3 (99.99%, Nippon Yttrium) were weighed at molar ratios of Ca:Sn:Eu:Y=2–x: 1–x: x:x (x=0, 0.1, 0.2, 0.3, 0.4, 0.5 and 0.6). Eu^{3+}-doped Ca_2SnO_4 with a composition of $Ca_{1.9}Eu_{0.2}Sn_{0.9}O_4$ was also prepared for reference. The powders were mixed in an agate mortar, pressed into pellets and placed on a platinum plate. The pellets were heated at 1400 °C for 12 h (cooling rate ~900 °C h^{-1}) and then powdered for XRD analysis. This procedure (pelletizing, heating and powdering) was repeated until no change in the XRD pattern was observed. The detailed sample synthesis procedures are reported in Ref. [5].

The pellet samples were then powdered and characterized by XRD analysis using Cu$K\alpha$ radiation and a graphite monochromator mounted on a powder diffractometer (Rigaku, RINT2000). The crystal structure parameters of $Ca_{2-x}Eu_xY_xSn_{1-x}O_4$ ($0 \le x \le 0.60$) and $Ca_{1.9}Eu_{0.2}Sn_{0.9}O_4$ were refined by Rietveld analysis of the powder XRD patterns (2θ=10–140° and a step width of 0.02°) using the program RIETAN-2000 [7].

The PL excitation and emission spectra of $Ca_{2-x}Eu_xY_xSn_{1-x}O_4$ ($0 \le x \le 0.60$) and $Ca_{1.9}Eu_{0.2}Sn_{0.9}O_4$ were measured at room temperature with a fluorescence spectrophotometer (Hitachi, F-4500) equipped with a 150 W xenon lamp as the excitation source.

2.2. Transmission electron spectroscopy and associated analysis

Samples of nominal compositions of Ca_2SnO_4 (nondoped), $Ca_{1.9}Eu_{0.2}Sn_{0.9}O_4$, $Ca_{1.8}Eu_{0.2}Y_{0.2}Sn_{0.8}O_4$ and $Ca_{1.5}Eu_{0.5}Y_{0.5}Sn_{0.5}O_4$, hereafter referred to as nondoped, Eu20, Eu20Y20, and Eu50Y50, respectively, were examined by TEM–EDX and TEM–EELS.

The sintered pellet samples were cut into sheets of $2 \times 2 \times 0.5$ mm^3, followed by dimpling at the center and Ar ion thinning to obtain thin areas transparent to high-energy incident electrons of TEM. TEM–EDX analysis was performed with a Hitachi H-800 TEM system (operated at 200 kV) equipped with an EDAX EDX system. The samples were also examined by EELS with a JEOL JEM2100 TEM system (operated at 200 kV) equipped with a Gatan Enfina 1000 spectrometer.

To determine the site occupancies of the rare-earth dopants, the statistical analysis method of electron channeling microanalytical data proposed by Rossouw et al. [8] was used. We measured 20–30 datasets for one crystal grain by slightly tilting the sample consecutively around low-index zone axes within a few degrees; two different crystal grains were examined for each sample. The beam spot size was 0.2 μm and the EDX recording time was 100 s for each acquisition to obtain statistically sufficient counts where the peak-to-background ratio was sufficiently large to minimize the error caused by the background fitting. The k-factors for Ca-K_α (3.7 keV) and Sn-L_α (3.4 keV) lines were calibrated using the EDXA data recorded under several kinematical diffraction (nonchanneling) conditions in the nondoped sample with the nominal composition assumed and averaged. Care was taken to obtain the EDX data at areas of similar thicknesses, that is, 100–150 nm, where electron channeling phenomena are strongly expected and X-ray emissions exhibit little significant difference in absorption effects within the thickness range. For the Eu-L_α (5.8 keV) and Y-K_α (14.9 keV) lines, the k-factors were calculated from the EDX data obtained under kinematical conditions assuming the nominal composition for each sample. Since the Sn-L_β line (3.7 keV) overlaps with the Ca-K_α line, which significantly affects the intensity estimation of the Ca-K_α line, the intensity of the Ca-K_α line was calibrated by subtracting a fraction (0.55) of the neighboring Sn-L_α intensity [9]. It was confirmed that the k values obtained are not very different from the theoretical estimations tabulated in the EDX analysis software attached to the system. The principle of the present analysis is described in Appendix A.

Since the O-K ELNES showed significant variation for the Eu50Y50 sample (as shown in Section 3.2), the extended energy-loss fine structure (EXELFS) of the O-K EELS was analyzed to examine the local atomic configuration around oxygen atoms [10]. To collect spectral intensities with sufficient signal-to-noise ratio, the spectrometer dispersion was set to 0.5 eV/channel, accumulating 1000 spectra within a single acquisition time of 2 s. During this prolonged data recording, spectral drifts caused by the external stray field were calibrated using an on-line drift cancellation program [11].

3. Results and discussion

3.1. XRD analysis and PL measurement

The result of the Rietveld analysis of Eu50Y50 is shown in Fig. 1 as an example. All peaks in the XRD patterns of $Ca_{2-x}Eu_xY_xSn_{1-x}O_4$ ($0 \le x \le 0.50$) and Eu20 were indexed to the orthorhombic cell of the Ca_2SnO_4 structure (space group: *Pbam* (no. 55)) [12]. According to previous reports [5], we refined the $Ca_{2-x}Eu_xY_xSn_{1-x}O_4$ crystal structure using the model of Eu substitution for Ca and Y substitution for Sn in the Ca_2SnO_4 structure. The refined crystal structure parameters of nondoped, Eu20Y20, Eu50Y50 and Eu20 are listed in Table S1 in the supplementary data. As shown in Fig. 2, the a-, b- and c-axis lengths of Eu50Y50 are, respectively, 0.48%, 1.6% and 2.8% larger than those of Ca_2SnO_4. The solid solubility limit of $0.50 < x < 0.60$ was slightly smaller than that of $Ca_{2-y}Eu_{2y}Sn_{1-y}O_4$ ($0.6 < 2y < 0.8$) [5]. $Ca_{0.8}Y_{2.4}Sn_{0.8}O_6$ peaks (rhombohedral, space group: $R\bar{3}$ (no. 148)) [13] appeared in the XRD pattern of the samples with x=0.6.

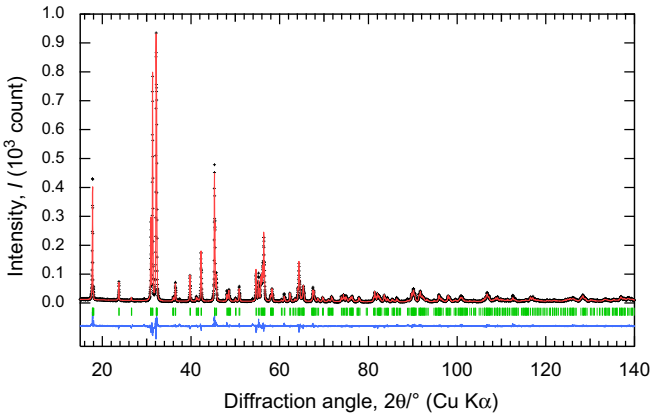

Fig. 1. Observed (crosses) and calculated (solid line) powder XRD patterns of Eu50Y50. Vertical lines show the Bragg peak positions. The difference is shown at the bottom of the figure.

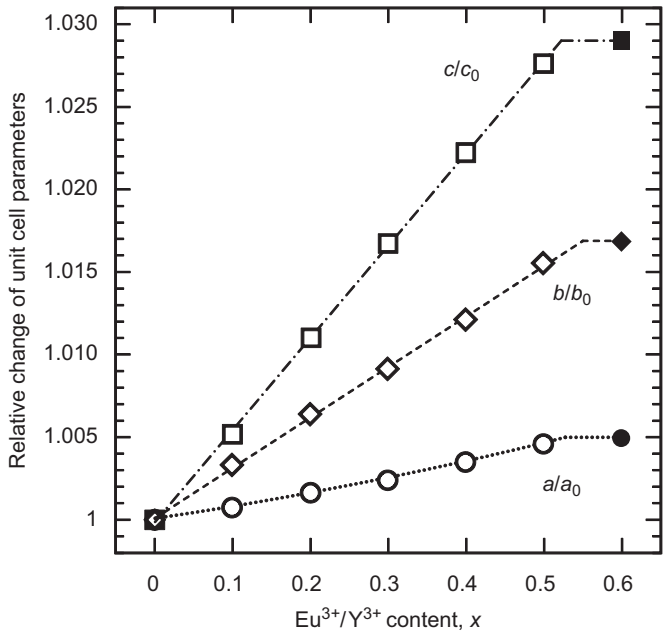

Fig. 2. Normalized unit cell parameters of $Ca_{2-x}Eu_xY_xSn_{1-x}O_4$ as a function of Eu^{3+}/Y^{3+} content (x).

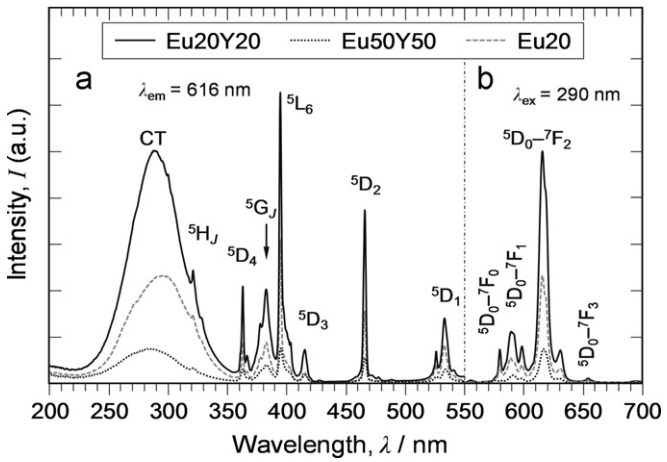

Fig. 3. PL excitation (a) and emission (b) spectra of Eu20Y20 (solid line), Eu50Y50 (dotted line) and Eu20 (dashed line). The excitation (λ_{ex}) and monitored (λ_{em}) wavelengths are 290 and 616 nm, respectively.

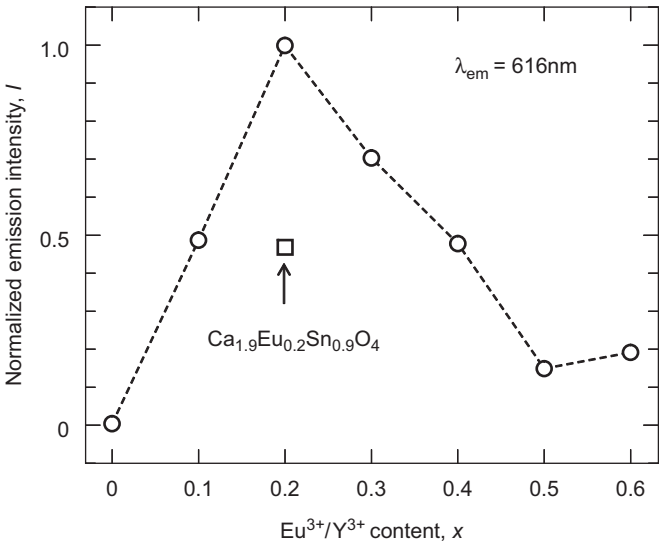

Fig. 4. Normalized PL intensities monitored at 616 nm as a function of Eu^{3+}/Y^{3+} content (x) of the samples. A square indicates the intensity of Eu20, which has the same Eu^{3+} content as Eu20Y20.

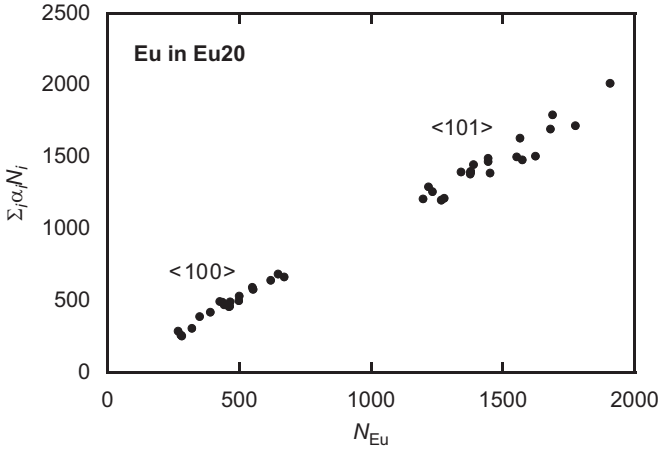

Fig. 5. Fit of N_{Eu} to $\Sigma_i \alpha_{ix} N_i$ (i=Ca or Sn) for sample Eu20, together with a linear fit to the data. The incident electron directions around which the sample orientation changes are indicated in the inset.

Fig. 3 shows the PL excitation and emission spectra of Eu20Y20, Eu50Y50 and Eu20. A broad excitation band at 290 nm attributed to the charge transfer and sharp excitation peaks at 310–550 nm attributed to the f–f transitions of Eu^{3+} ions were observed for both samples. Eu20Y20 and Eu20 showed sharp red emissions at around 616 nm due to the $^5D_0$–$^7F_2$ electric dipole transition of Eu^{3+} ions excited with a 290 nm light. The peak positions of the excitation and emission bands attributed to the f–f transitions of the Eu^{3+} ions remained almost unchanged with the various Y^{3+}/Eu^{3+} contents. On the other hand, the peak positions of the charge transfer absorption in the excitation spectra were shifted by co-doping of Y. Emission intensity is plotted against Eu^{3+}/Y^{3+} content (x) in Fig. 4. The maximum intensity was observed for Eu20Y20 and was around two-fold higher than that of Eu20, while the spectrum shapes of the co-doped samples scarcely changed with increasing the Y^{3+}/Eu^{3+} contents, as also show in Fig. 3. This suggests similar coordination environments of Eu^{3+} in the co-doping samples.

3.2. Site occupancies of rare-earth impurities

Fig. 5 shows the fits of N_{Eu} to $\Sigma_i \alpha_{ix} N_i$ (i=Ca or Sn) for the Eu20 sample, which show statistical accuracies of the experimental data. The plots for the other samples are provided in the supplemental data. Note that the count rate changes nearly by one order of magnitude with a change in the crystal orientation around the zone axis in each experiment, and the data points from the two different crystal grains generally lie on the same straight line in each sample, suggesting that the compositions of all the samples are uniform. The coefficients α_{ix} (i=Ca, Sn, x=Eu, Y) derived using Eq. (2), the site occupancies f_{ix} (Eq. (3)) of the impurities and the impurity concentrations c of all the samples are tabulated in Table 1. Scatters of the data points deviating from the straight line in Fig. 5 directly reflect the accuracy of each corresponding α_i.

The resulting compositions are shown in Table 2, together with those obtained by XRD–Rietveld analysis (supplemental data: Table S1). In Eu20, Eu^{3+} equally occupies the Ca^{2+} and Sn^{4+} sites ensuring the charge neutrality condition, which is consistent with the

Table 1
Derived parameters (defined in Appendix A) of the samples of $Ca_{2-x}Eu_xSn_{1-y}Y_yO_4$ where $(x, y)=(0.2, 0.0)$, $(0.2, 0.2)$ and $(0.5, 0.5)$, respectively, refer to Eu20, Eu20Y20 and Eu50Y50.

Sample	Dopant	α_{Ca}	α_{Sn}	f_{Ca}	f_{Sn}	c_x (x=Eu or Y)
Eu20	Eu	0.070 ± 0.008	0.119 ± 0.014	0.51 ± 0.07	0.49 ± 0.06	0.0065 ± 0.005
Eu20Y20	Eu	0.112 ± 0.010	0.093 ± 0.015	0.70 ± 0.06	0.30 ± 0.08	0.071 ± 0.006
	Y	0.050 ± 0.012	0.147 ± 0.019	0.40 ± 0.11	0.60 ± 0.11	0.079 ± 0.010
Eu50Y50	Eu	0.303 ± 0.013	0.298 ± 0.031	0.69 ± 0.05	0.31 ± 0.05	0.159 ± 0.007
	Y	0.107 ± 0.015	0.369 ± 0.034	0.39 ± 0.06	0.61 ± 0.05	0.149 ± 0.012

Table 2
Compositions of the evaluated samples of Eu20, Eu20Y20 and Eu50Y50. The values in brackets are XRD–Rietveld results.

Site	Element	Ca_2SnO_4 (nondoped)	Eu20	Eu20Y20	Eu50Y50
Ca	Ca	2.00	1.89 ± 0.01 (1.900(5))	1.77 ± 0.04 (1.798(6))	1.46 ± 0.04 (1.498(6))
	Eu	–	0.11 ± 0.01 (0.100(5))	0.15 ± 0.02 (0.202(6))	0.36 ± 0.02 (0.502(6))
	Y	–	–	0.08 ± 0.02 (0.0)	0.18 ± 0.02 (0.0)
Sn	Sn	1.00	0.91 ± 0.01 (0.900(5))	0.83 ± 0.04 (0.797(6))	0.54 ± 0.04 (0.498(6))
	Eu	–	0.09 ± 0.01 (0.100(5))	0.05 ± 0.02 (0.0)	0.14 ± 0.02 (0.0)
	Y	–	–	0.12 ± 0.02 (0.203(6))	0.32 ± 0.02 (0.502(6))
Total charge per chemical formula		0	$+0.010 \pm 0.025$	$+0.038 \pm 0.077$	$+0.086 \pm 0.108$

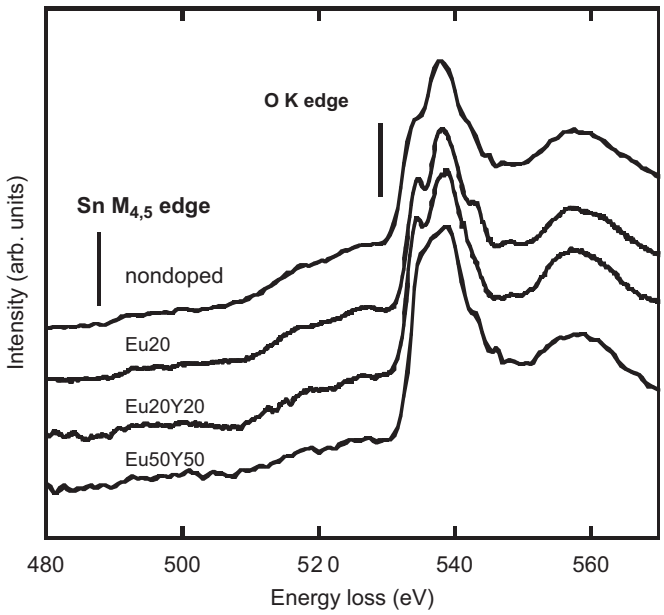

Fig. 6. Electron energy-loss spectra of O K and Sn $M_{4,5}$ for the present samples as indicated.

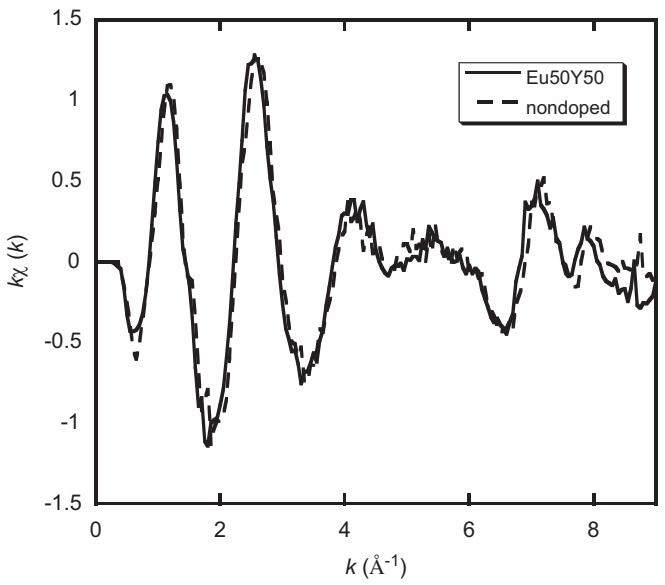

Fig. 7. EXELFS interference functions $k\chi(k)$ extracted from the O K EEL spectra of nondoped and Eu50Y50 samples. k stands for the wave number in unit of $Å^{-1}$.

results of XRD–Rietveld analysis. On the other hand, in the codoped samples, Eu^{3+} and Y^{3+} occupied the Ca^{2+} and Sn^{4+} sites at fractions of approximately 7:3 and 4:6, respectively, without resulting in a complete bias for a single site by a single element, which maintained the charge neutrality condition within the present experimental accuracies, as shown in the bottom row of Table 2. The f_{ix}'s of the codoped samples are nearly independent of dopant concentration.

3.3. Electron energy-loss spectroscopy

The ELNES of Ca-$L_{2,3}$, Y-$L_{2,3}$ and Eu-$M_{4,5}$ exhibited no dependence on dopant concentration. In addition, the results of high-angular resolution channeling enhanced EELS (HARECES) [14] of Y-$L_{2,3}$ and Eu-$M_{4,5}$ ELNES indicated that the rare-earth dopants were trivalent, independent of the type of atomic site occupied. On the other hand, Fig. 6 shows that O-K ELNES of the Eu50Y50 sample exhibited a blunt nature compared with that of the other samples, which can be caused by either local lattice distortions around oxygen or an increased concentration of dopant–oxygen pairs.

To confirm whether local lattice distortions around oxygen atoms are present, the extended energy-loss fine structures (EXELFSs) of the O-K edges of the nondoped and Eu50Y50 samples were compared. The EXELFS interference function, $\chi(k)$ was extracted in the same manner as in EXAFS analysis by subtracting the post-edge background from the oxygen K-shell EEL spectra recorded up to 900 eV and then normalizing the remaining signal

by the post-edge background. The origin of the wave number k was set at the inflection point of the edge onset [10]. The $k\chi(k)$'s of both samples are shown in Fig. 7, and indicates no appreciable changes in the local bond lengths except for a slight decrease in the wavelength of the main oscillating component, reflecting an increase in the lattice constants associated with the doping of oversized ions. It is thus considered that the blunt O-K ELNES of the Eu50Y50 sample is ascribed to the overlapping of multiple chemical states revealed by the increased dopant concentrations, rather than to local lattice distortions associated with the heavy doping.

4. Conclusions

The present electron channeling microanalysis directly confirmed that Eu^{3+} occupies both the Ca^{2+} and Sn^{4+} sites in the Eu20 sample ($Ca_{1.9}Eu_{0.2}Sn_{0.9}O_4$); however, in the codoped samples ($Ca_{2-x}Eu_xY_xSn_{1-x}O_4$, $x=0.2$ and 0.5), the site occupancies are slightly biased so that the dopant atoms preferentially occupy cation sites with an ionic radius larger than theirs. It should be emphasized here that while it is not favorable for some Eu^{3+} to go on the smaller Sn^{4+} site, this is still energetically better than creating Ca vacancies or any other of the possible charge balance mechanisms. This clearly explains the enhancement of PL intensity associated with the $^5D_0$–$^7F_2$ electric dipole transition of Eu^{3+} ions by co-doping with Y up to a certain concentration, although we presently found no specific reason for the start of PL intensity decrease at dopant concentrations larger than Eu^{3+}/Y^{3+} content $x=0.2$ other than the general concentration quenching. Nevertheless, it is clear that the present statistical analysis method for electron channeling microanalysis data will contribute to our better understanding of the mechanism of light emission in phosphor materials by impurity doping.

Supporting information

Tables of the refined crystal structure parameters and bond lengths, and the fits of N_x (x=Eu or Y) to $\Sigma_i\alpha_{ix}N_i$ (i=Ca or Sn) for the Eu20Y20, and Eu50Y50 samples (rest part of Fig. 5) are available as supplementary data at doi:10.1016/j.jssc.2010.07.26.

Acknowledgments

The present authors are grateful to Dr. S. Arai of EcoTopia Research Institute and to Prof. K. Hirose of Technical Institute of Tokyo for their assistance in EDX data recording. This work was supported in part by the Global COE Program "Materials Integration, Tohoku University" and a Grant-in-Aid for Scientific Research (KAKENHI) in Priority Areas (#474) "Atomic Scale Modification."

Appendix A

Electron channeling for orientations under or near strong diffraction conditions results in standing waves that peak at different sites in the crystal unit cell and move as the crystal orientation with respect to the incident electron beam is varied. This phenomenon is the basis of the atom location channeling enhanced microanalysis (ALCHEMI) technique first introduced by Taftø and Spence [15] for the determination of the location of minor species on atomic sites in the crystal structure. On the other hand, since the original ALCHEMI method is sensitive to several significant sources of error, the statistical ALCHEMI method was proposed by Rossouw et al. [8] in the case where a single impurity element may occupy multiple nonequivalent host sites to overcome the difficulties in the original method. This method is superior to the original ALCHEMI procedure in that the accuracies of the measurements can be readily estimated by statistically processing the data sets, consisting of 20–30 typical sampling points, obtained irrespective of the specific diffraction conditions at each measurement. The method was then extended to the case where the system contains multiple impurities.

The X-ray count N_x for impurity x (in the present case, x=Eu or Y) can be written in the following form as a function of X-ray count N_i of host element i (e.g., i=Ca or Sn),

$$N_x = \frac{c_x}{k_k}\sum_i \frac{f_i k_i N_i}{(n_i - \sum_x c_x f_{ix})} = \sum_i \alpha_{ix} N_i, \tag{1}$$

where

$$\alpha_{ix} = \frac{c_x}{k_k}\frac{f_i k_i}{(n_i - \sum_x c_x f_{ix})}, \tag{2}$$

where c_x is the concentration of impurity x, k_i is the k-factor of element i, n_i is the fraction of the cation site of element i among the total cation sites, and f_{ix} is the fraction of impurity x occupying the i-site. Many datasets of X-ray intensities from the cation elements (i.e., N_x, N_{Ca} and N_{Sn}) are collected by tilting a sample by a few degrees at the same spot. α_{ix} can be derived from Eq. (1) by a multivariate linear regression. Then, c_x and f_{ix} can be derived utilizing $\sum_i f_{ix}=1$ as

$$c_x = \sum_i \frac{\alpha_{ix} n_i}{(\sum_x \alpha_{ix} + k_i/k_x)}, \quad f_{ix} = \frac{\alpha_{ix} n_i}{c_x(\sum_x \alpha_{ix} + k_i/k_x)}. \tag{3}$$

Although the uncertainties in c_x and f_{ix} for multiple impurities have not been explicitly derived in Ref. [16] they are readily estimated from the error propagation principle:

$$(\delta c_x)^2 = \sum_i \left[-\frac{\alpha_{ix} n_i}{(\sum_x \alpha_{ix} + k_i/k_x)^2} + \frac{n_i}{(\sum_x \alpha_{ix} + k_i/k_x)}\right]^2 (\delta\alpha_{ix})^2, \tag{4}$$

$$(\delta f_{ix})^2 = \frac{1}{c_x^2}\left[-\frac{\alpha_{ix} n_i}{(\sum_x \alpha_{ix} + k_i/k_x)^2} + \frac{n_i}{(\sum_x \alpha_{ix} + k_i/k_x)}\right]^2 (\delta\alpha_{ix})^2 + \left(\frac{\delta c_x}{c_x^2}\right)^2 \left[\frac{\alpha_{ix} n_i}{(\sum_x \alpha_{ix} + k_i/k_x)}\right]^2. \tag{5}$$

Appendix B. Supporting information

Supplementary data associated with this article can be found in the online version at doi:10.1016/j.jssc.2010.07.026.

References

[1] A.J. Kenyon, Prog. Quantum Electron. 26 (2002) 225–284.
[2] Y.-C. Chen, Y.-H. Chang, B.-S. Tsai, Opt. Mater. 27 (2005) 1874–1878.
[3] H.M. Yang, J.X. Shi, M.L. Gong, J. Solid State Chem. 178 (2005) 917–920.
[4] R.D. Shannon, Acta Crystallogr. A32 (1976) 751–767.
[5] H. Yamane, Y. Kaminaga, S. Abe, T. Yamada, J. Solid State Chem. 181 (2008) 2559–2564.
[6] L. Jiang, C. Chang, D. Mao, C. Feng, Mater. Sci. Eng. B 103 (2003) 271–275.
[7] F. Izumi, T. Ikeda, Mater. Sci. Forum 321–324 (2000) 198–203.
[8] C.J. Rossouw, P.S. Turner, T.J. White, A.J. O'Cornner, Philos. Mag. Lett. 60 (1989) 225–232.
[9] A. Thompson (Ed.), X-ray Data Booklet, Center for X-ray Optics and Advanced Light Source, Lawrence Berkeley National Laboratory, 2001 Tables 1–3.

[10] Y. Kobayashi, S. Muto, C. Echer, T. Tanabe, J. Electron Microsc. 48 (1999) 525–529.
[11] Y. Sasano, S. Muto, J. Electron Microsc. 57 (2008) 149–158.
[12] M. Trömel, Z. Anorg. Allg. Chem. 54 (1969) 237–247.
[13] Y. Kaminaga, H. Yamane, T. Yamada, Acta Crystallogr. C62 (2006) i57–i58.
[14] K. Tatsumi, S. Muto, I. Nishida, J. Rusz, Appl. Phys. Lett. 96 (2010) 201911-1-3.
[15] J. Taftø, J.C.H. Spence, Ultramicroscopy 9 (1982) 243–248.
[16] P.S. Turner, T.J. White, A.J. O'Conner, C.J. Rossouw, J. Microsc. 162 (1991) 369–378.